Inorganic Chemistry

Article

pubs.acs.org/IC

Dioxo–Fluoroalkoxide Tungsten(VI) Complexes for Growth of WO_x Thin Films by Aerosol-Assisted Chemical Vapor Deposition

Richard O. Bonsu,[†] Hankook Kim,[‡] Christopher O'Donohue,[‡] Roman Y. Korotkov,[§] Khalil A. Abboud,[†] Timothy J. Anderson,[‡] and Lisa McElwee-White*[,†]

[†]Department of Chemistry, University of Florida, Gainesville, Florida 32611-7200, United States

[‡]Department of Chemical Engineering, University of Florida, Gainesville, Florida 32611-6005, United States

[§]Arkema Inc., 900 First Avenue, King of Prussia, Pennsylvania 19406, United States

Supporting Information

ABSTRACT: The soluble bis(fluoroalkoxide) dioxo tungsten(VI) complexes $WO_2(OR)_2(DME)$ [**1**, R = $C(CF_3)_2CH_3$; **2**, R = $C(CF_3)_3$] have been synthesized by alkoxide–chloride metathesis and evaluated as precursors for aerosol-assisted chemical vapor deposition (AACVD) of WO_x. The ^1H NMR and ^{19}F NMR spectra of **1** and **2** are consistent with an equilibrium between the dimethoxyethane (DME) complexes **1** and **2** and the solvato complexes $WO_2(OR)_2(CD_3CN)_2$ [**1b**, R = $C(CF_3)_2CH_3$; **2b**, R = $C(CF_3)_3$] in acetonitrile-d_3 solution. Studies of the fragmentation of **1** and **2** by mass spectrometry and thermolysis resulted in observation of DME and the corresponding alcohols, with hexafluoroisobutylene also generated from **1**. DFT calculations on possible decomposition mechanisms for **1** located pathways for hydrogen abstraction by a terminal oxo to form hexafluoroisobutylene, followed by dimerization of the resulting terminal hydroxide complex and dissociation of the alcohol. AACVD using **1** occurred between 100 and 550 °C and produced both substoichiometric amorphous WO_x and a polycrystalline $W_{18}O_{49}$ monoclinic phase, which exhibits 1-D preferred growth in the [010] direction. The work function (4.9–5.6 eV), mean optical transmittance (39.1–91.1%), conductivity (0.4–2.3 S/cm), and surface roughness (3.4–7.9 nm) of the WO_x films are suitable for charge injection layers in organic electronics.

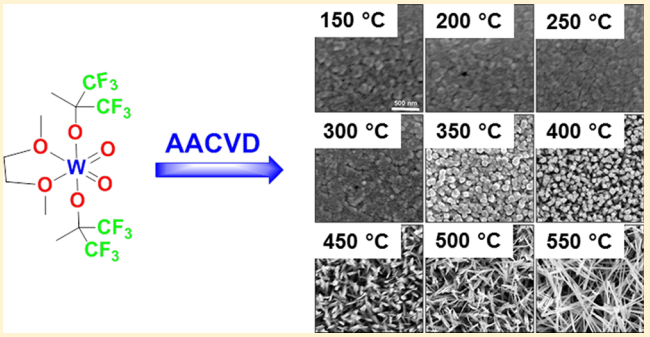

INTRODUCTION

The organic electronics industry has recently considered ultrathin transition metal oxides, such as TiO_2, V_2O_3, MoO_3 and WO_3, as charge-injection materials, which may minimize charge extraction and transport energy barriers that exist at device interfaces.[1−4] WO_{3-x} is an excellent candidate as a charge injection and transport layer material in organic electronics,[3,5−8] owing to its large and tunable work function (5.0–6.7 eV),[3,4,8−10] visible light transparency,[7,10,11] and mechanical and electrical robustness.[6,9,11,12] The work function varies from 5.0 to 6.7 eV[3,8] as a function of the stoichiometry and crystallinity, as WO_x can exist in several Magnéli phases, each with a different energy band structure.[13,14] Stoichiometric WO_3 is also known to be highly transparent and with low refractivity,[7] and the suboxides (W^{5+} and W^{4+}) are electrically semiconducting.[9,15] These tunable properties establish WO_x as an appropriate candidate for both hole-injection layers (HILs) at the anode and the electron-transporting layers (ETLs) at the cathode of organic light emitting diodes (OLEDs).[7,11] In addition, tungsten oxide is also a remarkable candidate for gas sensing applications due to its high sensitivity and robustness. In sensing experiments, $W_{18}O_{49}$ nanowires showed a higher response value to low concentration H_2S (1000 ppm) than WO_3 nanoparticles and nanoplatelets due to their large surface to volume ratio, and semiconducting properties.[16,17]

In spite of the attractive properties of WO_x, its processing for organic devices proves to be an unmet challenge. Typically, thermal evaporation of WO_3 samples requires elevated growth temperatures (>900 °C)[18,19] that may be detrimental to device components. CVD has the capability for lower temperature growth of WO_x by variation of the precursor structure. Furthermore, CVD offers the potential for conformal and uniform *in situ* growth on large-area substrates. Aerosol-assisted CVD (AACVD), in particular, permits enhanced mass transport rates compared to transpiration, which allow for faster growth, milder reactor operating conditions,[20−22] and a wider choice of precursors. In AACVD, solubility of the precursor in an appropriate solvent is required for aerosol production and transport, but this requirement is less of a limitation on precursor selection than the need for volatility in conventional CVD. Design of single-source precursors for AACVD and LPCVD of WO_x has focused on complexes with alkoxide and related ligands such as tungsten pentaethoxide

Received: May 20, 2015
Published: July 14, 2015

DOI: 10.1021/acs.inorgchem.5b01124
Inorg. Chem. 2015, 54, 7536–7547

$[W(OEt)_5]$,[23,24] tungsten(VI) oxo complexes with alkoxide, siloxide, aryloxide, or salicylate ancillary ligands,[25−27] complexes of the type $WO(OR)_3L$ [R = ^{t}Bu, ^{i}Pr, L = acac, hfac, 2-(dimethylamino)ethanol],[28,29] and most recently the tungsten(VI) oxo−fluoroalkoxide derivatives.[30,31]

Our previous studies using $WO[OC(CH_3)_2CF_3]_4$ (**3**) and $WO[OC(CF_3)_2CH_3]_4$ (**4**) for growth of WO_x materials were consistent with gas phase decomposition of these tungsten(VI) mono-oxo alkoxide precursors to yield tungsten(VI) dioxo intermediates.[30] Following pyrolysis of **3** and **4**, the respective alcohols and fluorinated alkenes that would be generated by conversion of an alkoxide ligand to an oxo could be detected in the volatile products by gas chromatography−mass spectrometry (GC−MS). For instance, generation of hexafluoro-*tert*-butanol and hexafluoroisobutylene were obtained from **4**. The same fragmentation products were observed by mass spectrometry of neat samples of **3** and **4**, along with the corresponding protonated dioxo ions (e.g., $[WO(OC(CF_3)_2CH_3)_2(OH)]^+$ from **4**). To the extent that the gas phase ion chemistry observed in mass spectrometry models thermal decomposition,[32,33] these products are consistent with initial formation of tungsten(VI) dioxo intermediates $WO_2[OC(CF_3)_2CH_3]_2$ (**1a**) during film deposition, eq 1.

$$\underset{\mathbf{4}}{WO[OC(CF_3)_2CH_3]_4} \xrightarrow{\Delta} \underset{\mathbf{1a}}{WO_2[OC(CF_3)_2CH_3]_2} + H_2C{=}C(CF_3)_2 + HOC(CF_3)_2CH_3 \quad (1)$$

Precedent for conversion of alkoxide to oxo ligands can be found in studies of related transition metal complexes. Loss of isobutylene and *tert*-butanol was observed upon solid state thermolysis of $M[OSi(O^tBu)_3]_4$ (M = Ti, Zr, Hf) complexes to form $MO_2{\cdot}4SiO_2$.[34,35]

In view of the evidence that W(VI) dioxo complexes are generated as intermediates during the thermal decomposition of **3** and **4**, it became of interest to explore the W(VI) dioxo complexes themselves as precursors for the growth of WO_x materials. Complexes of the type WO_2L_2 (L = 2,4-pentanedionate, 1,1,1-trifluoro-2,4-pentanedionate, and 1-benzoylacetonate) have been reported to afford pure WO_3 and Pt/WO_3 films by photodeposition[36,37] but to our knowledge, dioxo complexes have not been explored as precursors for conventional CVD or AACVD of WO_x films. Due to the interest in continued development of precursors for deposition of high quality WO_x thin films for the electronics industry, we have begun to explore the deposition chemistry of tungsten dioxo complexes. Here, we report syntheses, characterization, and deposition studies for the soluble tungsten(VI) complexes $WO_2[OC(CF_3)_2CH_3](DME)$ (**1**) and $WO_2[OC(CF_3)_3](DME)$ (**2**) as single-source precursors for AACVD of WO_x.

EXPERIMENTAL SECTION

General Procedure. All manipulations were performed under an inert atmosphere using either glovebox or standard Schlenk techniques. All chemicals used were of reagent grade. Methylene chloride and toluene (Fisher Scientific) were purified using an MBraun MB-SP solvent purification system and stored over activated 3 Å molecular sieves. Diethyl ether was distilled from sodium/benzophenone and stored over activated 3 Å molecular sieves. Anhydrous 1,2-dimethoxyethane (Sigma-Aldrich), hexamethyldisiloxane (Sigma-Aldrich), and benzene-d_6 (Cambridge Isotopes) were stored over 4 Å molecular sieves. NaH, WCl_6 (Sigma-Aldrich), $HOC(CF_3)_2CH_3$ (SynQuest Laboratories), and $HOC(CF_3)_3$ (Matrix Scientific) were used as received. $WOCl_4$[38] (**5**), $WO_2Cl_2(DME)$[39] (**6**), $NaOC(CF_3)_2CH_3$[40] (**7**), and $NaOC(CF_3)_3$[40] (**8**) were synthesized as reported in the literature. NMR spectra were recorded on a Varian Mercury 300BB (300 MHz) spectrometer using residual protons from deuterated solvents for reference. Elemental analyses were performed by the University of Florida analytical service. Mass spectra were obtained on a Thermo Scientific Trace GC DSQ equipped with a direct insertion probe (DIP) using chemical ionization with methane as the reagent gas. The TGA analyses were run under nitrogen using a Mettler TGA/SDTA 851e with a crimped 40 μL aluminum pan, which was heated at 10 °C/min to 600 °C.

Synthesis of $WO_2[OC(CF_3)_2CH_3]_2(DME)$ (1). In the glovebox, freshly synthesized $WO_2Cl_2(DME)$ (**6**, 7.45 mmol; 2.80 g) was placed in a 250 mL Schlenk flask containing a stir bar, and 1,2-dimethoxyethane (40 mL) was added. The reaction mixture was stirred until it formed a translucent solution. $NaOC(CF_3)_2CH_3$ (**7**, 14.90 mmol; 3.20 g) dissolved in 30 mL of DME was added dropwise using an addition funnel to a stirring solution of **6** in DME. As addition of the DME solution of **7** to that of **6** progressed, the original translucent solution of **6** changed to blue, then a pale blue-white color. The reaction mixture was transferred to the Schlenk line and refluxed for 24 h. The solution turned whitish within the first hour of refluxing and then changed to yellowish-brown upon further refluxing for 24 h. In the glovebox, the mixture was filtered through Celite to yield a yellowish-brown solution. The filtrate was transferred back to the Schlenk line and the solvent removed under vacuum leaving a dense oily residue. Toluene (40 mL) was cannula transferred into the Schlenk flask with the residue and stirred. Again, the volatiles were removed to form a yellow-brown solid in 63% yield. The crude product was sublimed at 120−130 °C (300−350 mTorr) to afford a pale yellow to brown waxy solid. Yield: 1.32 g, 38%. ^{1}H NMR (DMSO-d_6, 25 °C): δ 3.43 (s, 2H, OCH_2), 3.24 (s, 3H, OCH_3), 1.63 (s, 3H, CH_3). $^{13}C\{^1H\}$ NMR (CD_2Cl_2, 25 °C): δ 124.56 (q, CF_3, $^1J_{C-F}$ = 288.0 Hz), 81.83 (septet, $C(CF_3)_2CH_3$ $^2J_{C-F}$ = 28.0), 71.88 (s, OCH_3), 64.41 (s, OCH_2), 16.24 (s, CH_3). ^{19}F NMR (DMSO-d_6, 25 °C): δ −77.83 (s, $C(CF_3)_2CH_3$). Anal. Calcd for $WO_5C_{16}H_{12}F_{24}$: C, 21.57; H, 2.41. Found: C, 21.51; H, 2.01%. Single crystals for X-ray crystallographic data collection grew upon storage of a toluene solution of **1** at −4 °C.

Synthesis of $WO_2[OC(CF_3)_3]_2(DME)$ (2). Compound **2** was synthesized following the same procedure as that for **1**, starting with $WO_2Cl_2(DME)$ (**6**, 1.23 mmol; 0.46 g) and $NaOC(CF_3)_3$ (**8**, 2.46 mmol, 0.64 g). A biphasic bluish-white solution obtained upon addition of the two starting materials was refluxed for 24 h. The reaction mixture formed a homogeneous white color within 1 h of refluxing, which persisted after 24 h. The crude product was isolated in 55% yield and sublimed at 80−90 °C (150−200 mTorr) to obtain a white fluffy solid. Yield: 0.47 g; 25%. ^{1}H NMR (DMSO-d_6, 25 °C): δ 3.43 (s, 2H, OCH_2), 3.24 (s, 3H, OCH_3). $^{13}C\{^1H\}$ + $^{19}F-^{13}C$ gHMBC NMR (CD_2Cl_2, 25 °C): δ 65.9 (OCH_2), 72.3 (OCH_3), 82.5 ($C(CF_3)_3$), 121.3 (CF_3). ^{19}F NMR (DMSO-d_6, 25 °C): δ −71.64. Anal. Calcd for $WO_6C_{12}H_{10}F_{18}$: C, 18.57; H, 1.30. Found: C, 18.58; H, 1.17%. Single crystals for X-ray crystallographic data collection grew upon storage of a toluene solution of **2** at −4 °C.

Crystallographic Structure Determination of 1 and 2. X-ray intensity data for **1** and **2** were collected at 243 and 100 K, respectively, on a Bruker DUO diffractometer using Mo Kα radiation (λ = 0.71073 Å) and an APEXII CCD area detector. Raw data frames were read by the program SAINT[41,42] and integrated using 3D profiling algorithms. The resulting data were reduced to produce *hkl* reflections and their respective intensities and estimated standard deviations. The data were corrected for Lorentz and polarization effects, and numerical absorption corrections were applied based on indexed and measured faces. The structure for **1** was solved and refined in SHELXTL2013,[41] using full-matrix least-squares refinement. The non-H atoms were refined with anisotropic thermal parameters, and all of the H atoms were calculated in idealized positions and refined riding on their parent atoms. The structure of complex **1** is located on a 2-fold rotation axis of symmetry, thus the asymmetric unit consists of half of it. Two CF_3 groups in **1** were disordered, and each was refined in two parts. In the final cycle of the refinement of **1**, 2421

DOI: 10.1021/acs.inorgchem.5b01124
Inorg. Chem. 2015, 54, 7536−7547

reflections (of which 1760 are observed with $I > 2\sigma(I)$) were used to refine 137 parameters, and the resulting R_1, wR_2, and S (goodness of fit) were 3.17%, 6.86%, and 1.135%, respectively. The refinement was carried out by minimizing the wR_2 function using F^2 rather than F values. R_1 is calculated to provide a reference to the conventional R value, but its function is not minimized. The structure for **2** was solved and refined in SHELXTL6.1,[42] using full-matrix least-squares refinement. The non-H atoms were refined with anisotropic thermal parameters, and all of the H atoms were calculated in idealized positions and refined riding on their parent atoms. The three CF_3 groups on C9 were disordered and were refined in two parts with their site occupation factors dependently refined to 0.553(9) and 0.447(9), respectively. In the final cycle of the refinement of **2**, 5092 reflections (of which 4885 are observed with $I > 2\sigma(I)$) were used to refine 324 parameters, and the resulting R_1, wR_2, and S (goodness of fit) were 3.48%, 8.08%, and 1.212, respectively. The refinement was carried out by minimizing the wR_2 function using F^2 rather than F values. R_1 is calculated to provide a reference to the conventional R value, but its function is not minimized.

Deposition and Characterization of WO_x Materials. The solid precursor **1** was dissolved in either diglyme or DME (0.034 M) under N_2, and the solution was taken up into a 10 mL gastight syringe. The solution was introduced into an ultrasonic nebulizer (1.44 MHz) using a syringe pump at a rate of 4 mL/h, where it was aerosolized and transported by N_2 (1000 sccm, 99.999% purity, Airgas) to the reaction zone. In some instances, water vapor was introduced into the reaction chamber by bubbling 50 sccm N_2 through deionized (DI) water maintained at a constant temperature and pressure of 5 °C and 760 Torr, respectively (Figure S1 in the Supporting Information). In such cases, only 950 sccm N_2 was used for precursor transport to maintain mole fractions. Under these conditions, the estimated water vapor partial pressure in the system was 0.15 Torr, approximately 9 times that of the precursor. ITO (150 nm) coated borosilicate glass and plain borosilicate glass substrates resting on a pedestal-type SiC-coated graphite susceptor were heated by radio frequency (RF) to susceptor temperatures between 100 and 550 °C. The deposition reactor operating pressure was maintained at 350 Torr by a downstream throttling valve. When using DME as a solvent, the system pressure was maintained at 700 Torr to prevent premature solvent vaporization. The typical deposition time was 150 min. X-ray photoelectron spectroscopy (XPS, PerkinElmer PHI5100) was employed for elemental analyses. The samples were sputtered by 500 eV Ar^+ for 10 min to remove surface contaminants. Plan-view and cross-sectional images of grown materials were acquired using a field emission scanning electron microscope (FESEM, FEI Nova NanoSEM 430) to determine the surface morphology and the material thickness. X-ray diffraction (XRD, Panalytical X'pert Pro) was used to obtain crystallographic information. The work function and the valence band structure of the films were measured by UV photoelectron spectroscopy (UPS, PerkinElmer PHI5000 Versa probe2) after 5 min Ar^+ sputtering. Atomic force microscopy (AFM, Veeco Dimension 3100) was employed to measure the surface roughness. Conductivities and visible light transmittances of tungsten oxide materials on bare glass substrates were evaluated and measured with 4-point probe (Veeco FPP-100) and UV–vis spectroscopy (Shimadzu UV-1650PC). The details of the characterization methods are reported elsewhere.[43]

RESULTS AND DISCUSSION

Precursor Design. Growth of high work function and optically transparent WO_x thin films that possess acceptable conductivities requires appropriate levels of O incorporation. Precursors bearing terminal oxo ligands on the W(VI) center are appealing candidates, because the core structure of a precursor molecule can facilitate control of film stoichiometry and phase.[44,45] Use of bulky substituents is a common strategy in precursor design because steric bulk favors formation of monomeric complexes[46−48] by shielding the metal center from oligomer formation through bridging ligands. Decomposition pathways that permit oxygen incorporation can also be facilitated in sterically crowded molecules.[49,50] Fluorinated alkoxide ligands provide the additional benefit of behaving as repelling hard spheres that display reduced dispersion forces between their molecules, thereby increasing the volatility of the compound, a crucial precursor property for volatilization in bubblers for conventional CVD.[46,51]

For AACVD applications, precursor solubility and stability in a suitably volatile solvent are required. To ensure solubility of the final precursor molecule and stabilize the highly electron poor W(VI) center, a coordinating solvent such as DME can be advantageous. These considerations led to the bis(fluoroalkoxide) dioxo tungsten(VI) complexes $WO_2(OR)_2(DME)$ [**1**, R = $C(CF_3)_2CH_3$; **2**, R = $C(CF_3)_3$] as the target precursors.

Synthesis. Attempts to synthesize **1** and **2** by reaction of the commercially available WO_2Cl_2 with the alkoxide ligands in DME resulted in no product formation, even after refluxing the reaction mixture for several days. The soluble derivative $WO_2Cl_2(DME)$[39] (**6**) was found to be a more convenient starting material. Upon refluxing a solution of **6** with sodium fluoroalkoxide **7** or **8**, the reaction proceeded to afford **1** or **2** through a chloride–alkoxide exchange process (Scheme 1).

Scheme 1. Synthesis of 1 and 2

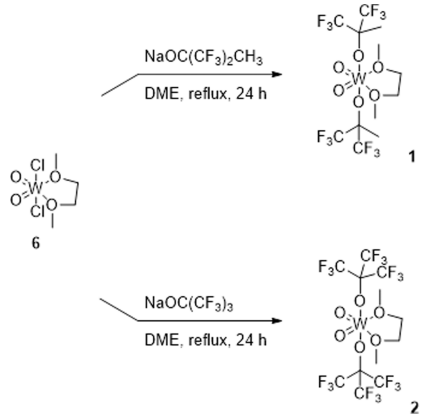

Complexes **1** and **2** were sufficiently volatile for sublimation, both as a purification method and for volatilization in CVD. Product **1** sublimed between 120 and 130 °C (300–350 mTorr) to afford a yellowish-brown waxy solid while **2** sublimed between 80 and 90 °C (150–200 mTorr) to yield a white fluffy solid. Like the starting material $WO_2Cl_2(DME)$, **1** and **2** are very soluble in THF, DME, DMSO, acetone, acetonitrile, and diglyme. Their solubility in methylene chloride is exceptionally high. Complex **1** has good solubility in benzene and toluene, whereas **2** is only slightly soluble. The two compounds exhibit less sensitivity to air than the mono-oxo complexes $WO[OC(CH_3)_2CF_3]_4$ (**3**) and $WO[OC(CF_3)_2CH_3]_4$ (**4**).[30] The solid complexes **1** and **2** can be exposed to air for over 48 h without decomposition and can be stored in a vial under air.

NMR Characterization. ^1H NMR and ^{19}F NMR spectra of **1** and **2** obtained at room temperature in DMSO-d_6 indicate symmetry equivalence of the fluoroalkoxide ligands (Figures S2–S5 in the Supporting Information). NMR spectra were obtained in additional solvents to study the solution dynamics of **1** and **2** (Figures S6–S10 in the Supporting Information). The ^1H NMR spectra recorded in CD_2Cl_2, C_6D_6, and CD_3CN

DOI: 10.1021/acs.inorgchem.5b01124
Inorg. Chem. 2015, 54, 7536−7547

at room temperature show resonances for free DME, suggesting that the coordinated DME is labile in solution. However, the proton and fluorine signals for **1** and **1b** in the alkoxide regions of solutions of **1** in CD_3CN (Scheme 3) are indistinguishable at

Scheme 2. Equilibrium between 1 and 2 and the Acetonitrile Complexes 1b and 2b in Solution

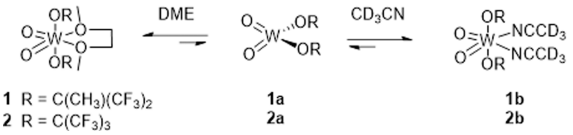

Scheme 3. Thermolysis of 1 and 2

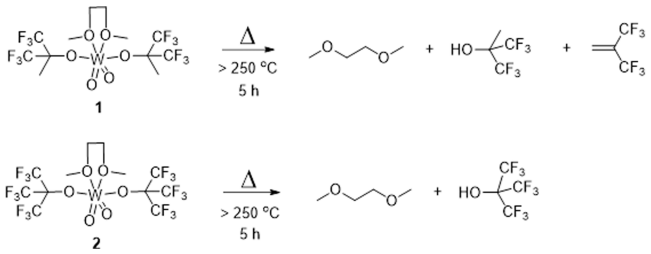

those temperatures (Figures 1a and 1b). In contrast, the ^{19}F NMR spectrum of **2** in the same solvent at room temperature displays two resonances corresponding to complex **2** and its acetonitrile derivative $WO_2[OC(CF_3)_3]_2(NCCD_3)_2$ **2b** (Figure 1d). The above observations are consistent with equilibration of **1** and **2** with the acetonitrile complexes **1b** and **2b** via the coordinatively unsaturated complexes **1a** and **2a** (Scheme 2). Additional support for the exchange of acetonitrile for DME in these samples is found in the ESI-MS obtained from solutions of **1** in acetonitrile. An intense signal at m/z = 660.50 can be assigned to the (bis)acetonitrile complex $\mathbf{1b}^+$.

Dissociation of coordinated DME in solutions of related tungsten dioxo complexes has been previously reported. The DME ligand in $WO_2Cl_2(DME)$[39] (**6**) was determined to be labile, and exchange with solvent was observed in both THF and acetonitrile. Only partial exchange occurred in acetonitrile, whereas complete exchange of DME for THF occurred in the THF solution. Likewise, the coordinated DME in $WO_2(OSi(O^tBu)_3)_2(DME)$ was reported to dissociate in solution.[52] Analogously, the DME in **1** and **2** appears to be largely replaced by solvent in solutions of THF-d_8 or acetone-d_6 whereas only partial substitution was observed in CD_2Cl_2, C_6D_6, or CD_3CN at room temperature. Unexpectedly, there was no DME dissociation or solvent exchange in samples of **1** or **2** in DMSO-d_6 at room temperature. However, the appearance of new ^1H and ^{19}F NMR signals upon heating samples of **2** to 80 °C in DMSO-d_6 (Figure S11 in the Supporting Information) is consistent with formation of the DMSO adducts.

Variable temperature ^1H NMR of the solutions of **1** and **2** in CD_3CN reveals that signals for the bound DME diminish and finally disappear, at approximately 25 and 70 °C in **1** and **2**, respectively (Figures 1a and 1c). The corresponding ^{19}F NMR spectrum of **2** shows broadening and coalescence of the fluorine signals for **2** and **2b** in solution above 70 °C (Figure 1d). As observed for $WO_2(OSi(O^tBu)_3)_2(DME)$,[52] complexes **1** and **2** are susceptible to decomposition in most coordinating solvents and upon heating of the pure compounds above room temperature as evident in the thermogravimetric analyses (TGA) in Figure 4. This lability of the complexes is consistent with the presence of the free fluoroalkoxides and decomposed compounds in the NMR samples.

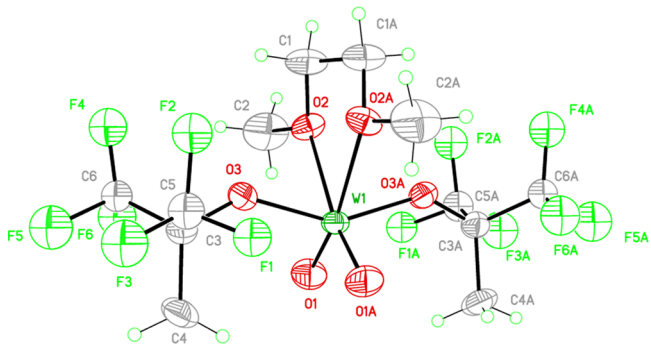

Figure 2. Displacement ellipsoid diagram of the molecular geometry of **1** drawn at 40% probability.

X-ray Structure Determination of 1 and 2. The structures of **1** and **2** were determined crystallographically, and their thermal ellipsoid diagrams are shown in Figures 2 and 3, respectively. The structural data confirm that **1** and **2** exist as monomers in the solid state and possess similar distorted octahedral geometries about their W(VI) centers. As expected for d^0 dioxo complexes,[53] the two oxo ligands are *cis* to one another and each is *trans* to a weakly donating oxygen of the DME ligand.

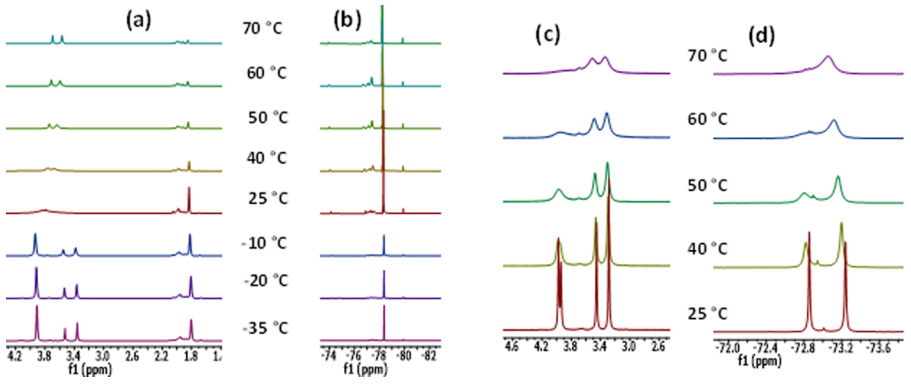

Figure 1. (a) ^1H NMR spectrum of **1**, (b) ^{19}F NMR spectrum of **1**, (c) ^1H NMR spectrum of **2**, and (d) ^{19}F NMR spectrum of **2** in CD_3CN showing signals from the DME and fluoroalkoxide regions.

DOI: 10.1021/acs.inorgchem.5b01124
Inorg. Chem. 2015, 54, 7536−7547

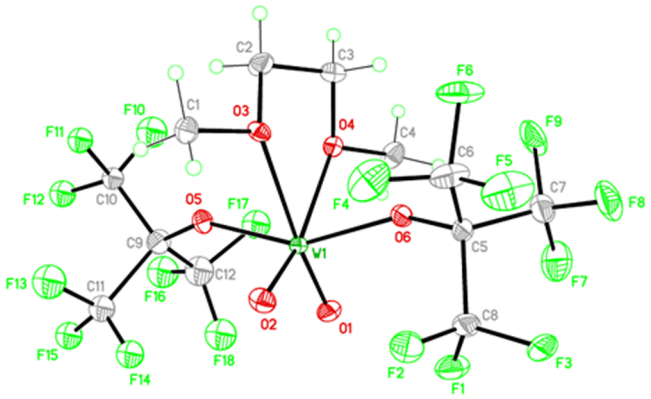

Figure 3. Displacement ellipsoid diagram of the molecular geometry of **2** drawn at 40% probability.

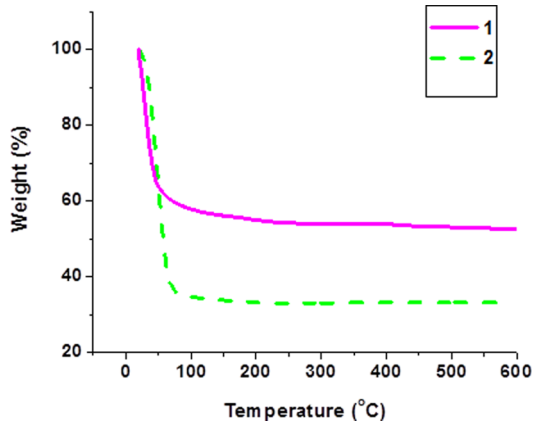

Figure 4. TGA of **1** and **2**.

In the context of the distorted octahedral structures of **1** and **2**, the two oxo ligands and the two coordinated oxygen atoms of the DME are defined to bind equatorially and in plane with the W atom. The two fluorinated *tert*-butoxide ligands bind at the two apical positions of the W to complete the octahedral coordination sphere. As in the isomorphous starting material $WO_2Cl_2(DME)$, the two terminal oxo ligands are *cis* to each other with bond lengths of 1.69(1) Å in both.[39] In complex **1**, the two terminal W═O moieties have bond lengths of 1.694(4) Å, whereas these are 1.707(5) and 1.711(5) in **2** (Table 1).

Distortions from a regular octahedron arise from the sterically bulky fluorinated *tert*-butoxide ligands that are slightly bent toward the plane of the bound DME ligand. A similar distortion of the H−Mo−H angle of the apical hydrides in $[MoO_2H_4]^{2-}$ has been studied computationally at the EHT level and attributed to strengthening of the metal−oxo π-bonding as the Mo−H bonds bend away from the *cis*-MoO_2 moiety.[33] In the simpler hydride system, the extent of the distortion was attributed to interplay between σ- and π-bonding, a situation which is further complicated in **1** and **2** by the steric difference between the alkoxide groups. The results for **1** and **2** are consistent with the steric demand as the angle O3−W1−O3A is more distorted (149.4(2)°) in **1** as compared to the larger perfluoro-*tert*-butoxide complex **2**, which has a somewhat less bent O5−W1−O6 bond angle of 152.9(2)° (Table 1).

Other notable features of **1** and **2** are the strong *trans* influence exerted by the oxo ligands over the chelated DME.

Table 1. Selected Bond Lengths (Å) and Angles (deg) for Compounds 1 and 2

bond parameter	1	bond parameter	2
W1−O1 (W1−O1A[a])	1.694(4)	W1−O1	1.707(5)
W1−O2 (W1−O2A)	2.299(4)	W1−O2	1.711(5)
W1−O3 (W1−O3A)	1.940(4)	W1−O3	2.268(5)
C3−O3 (C3A−O3A)	1.379(7)	W1−O4	2.270(5)
C3−C5 (C3A−C5A)	1.535(7)	W1−O5	1.964(5)
C1−O2 (C1A−O2A)	1.424(7)	W1−O6	1.959(5)
O1−W1−O1A	103.6(3)	O1−W1−O2	103.9(3)
O1−W1−O3	99.1(2)	O1−W1−O5	98.0(2)
O1−W1−O3A	99.7(2)	O1−W1−O6	98.0(2)
O1A−W1−O3	99.7(2)	O2−W1−O5	98.9(2)
O1A−W1−O3A	99.1(2)	O2−W1−O6	98.3(2)
O3 −W1−O3A	149.4(2)	O5−W1−O6	152.9(2)
W1−O3−C3	138.3(3)	W1−O5−C9	144.9(5)
W1−O3A−C3A	138.3(3)	W1−O6−C5	146.4(4)
O2−W1−O2A	70.20(18)	O3−W1−O4	71.5(2)

[a] $-x$, $1+y$, $0.5-z$.

This effect is prominent in **1** as the bond distances of the two terminal W−O bonds are both slightly shorter than in **2** and typical for terminal W−O bond lengths of complexes bearing hexafluoro-*tert*-butoxide ligands.[30] The bond distances [1.694(2) Å] are within the range expected for a bond order of three, which suggests that each oxo moiety enjoys maximum overlap with W orbitals with little or no competition from other oxo moiety for the same orbitals of the W atom. Also notable is the tight bite angle of the DME ligands (70.20(18) and 71.5(2)° in **1** and **2**, respectively).

Thermogravimetric Analysis of 1 and 2. The TGA data suggest that both **1** and **2** undergo a facile decomposition process, which initiates at room temperature and completes between 70 and 80 °C to yield WO_x matrices that maintain constant mass until 600 °C, the highest temperature studied (Figure 4). The residual masses at 600 °C are 53% and 33% in **1** and **2**, respectively. The volatile products lost during the TGA are presumably those identified following thermolysis of neat samples of **1** and **2**. These volatile byproducts were determined by GC−MS or NMR to be DME, hexafluoro-*tert*-butanol, and hexafluoroisobutylene from **1**. DME and perfluoro-*tert*-butanol were obtained from **2** (Figures S12−S21 in the Supporting Information). If the onset temperatures for decomposition of **1** and **2** during TGA are indicative of their reactivity under deposition conditions, then deposition of WO_x materials by CVD should occur at moderate temperatures for both precursors.

Mass Spectrometry of 1 and 2. Fragment ions generated by mass spectrometry have been shown to correlate well with precursor decomposition during CVD,[32,33] although care must be taken in the interpretation because CVD gives rise to neutral fragments through thermal processes whereas ionic species are produced in MS. Table 2 summarizes the m/z values and relative abundances of selected ions (See Table S2 in the Supporting Information for detailed data) observed upon direct insertion probe chemical ionization mass spectrometry (DIPCI-MS) of **1** and **2**.

The molecular ions are present only in small abundances for both **1** and **2**, suggesting that these thermally sensitive compounds are also sensitive to fragmentation upon ionization. The ions $\mathbf{1}^+$ and $\mathbf{2}^+$ undergo rapid loss of DME to generate $\mathbf{1a}^+$ and $\mathbf{2a}^+$, as the most abundant W containing fragments in the

DOI: 10.1021/acs.inorgchem.5b01124
Inorg. Chem. 2015, 54, 7536−7547

Table 2. Summary of the *m/z* Values and Relative Abundances for Positive Ion DIPCI Mass Spectra of 1 and 2

compound (MW)		ion	*m/z*	rel abundance[a] (%)
1 (668)	**1a**$^+$	$[M - DME]^+$	577.06	3
		$[HOCCH_3(CF_3)_2 + H]^+$	183.06	20
		$[DME + H]^+$	91.07	100
		$[HCC(CF_3)_2]^+$	163.07	17
2 (776)	**2a**$^+$	$[M - DME]^+$	686.90	7
		$[HOC(CF_3)_3 + H]^+$	237.00	100
		$[DME + H]^+$	91.07	39

[a]Relative abundances were calculated by adjusting peak intensities relative to the highest peak normalized to 100%.

mass spectra of **1** and **2**, respectively. Loss of DME in the mass spectra is consistent with the NMR and TGA data described above.

The presence of high intensity peaks for the protonated fluoro alcohols $[HOC(CF_3)_2CH_3 + H]^+$ and $[HOC(CF_3)_3 + H]^+$, which amount to 20% in **1** and 100% in **2**, suggests pathways involving W−O bond cleavage. Generation of fluoroisobutylene fragments from **1** is likely the result of concomitant C−O and C−H bond cleavage. These results are consistent with the observation of $[HOC(CH_3)_2CF_3 + H]^+$, $[HOC(CF_3)_2CH_3 + H]^+$, and fluoroisobutylene species in the positive ion DIPCI-MS spectra of the closely related complexes $WO[OC(CH_3)_2CF_3]_4$ (**3**) and $WO[OC(CF_3)_2CH_3]_4$ (**4**).[30]

Thermolysis of 1 and 2. To further investigate the fragmentations observed in the MS of **1** and **2**, neat samples of these compounds were heated above 250 °C for 5 h under flowing argon (1 atm) and their volatiles condensed at −78 °C. The condensate was dissolved in suitable solvents and analyzed by GC−MS or NMR. Scheme 3 highlights the abundant vapor phase species produced during thermolysis of **1** and **2**.

In both compounds, signals corresponding to DME and the corresponding fluorinated alcohol were present in the ^{1}H NMR and ^{19}F NMR spectra (Figures S15−S17, S20, and 21 in the Supporting Information). The presence of these fragments is further confirmed by GC−MS of the volatile residues from **1** and **2** (Figures S12−S14, S18, and S19 in the Supporting Information). Hexafluoroisobutylene fragments were also detected in both ^{1}H NMR and ^{19}F NMR spectra (Figures S15 and S16 in the Supporting Information) and the GC−MS (Figures S12 and S13 in the Supporting Information) of volatile species from **1** as well as DIPCI-MS using neat samples of **1** (Table 2).

DFT Calculations. Elimination of DME, fluoroisobutylene, and fluorinated alcohol from **1** has been computationally examined, and the lowest energy pathway found in the calculations is summarized in Figure 5. Detailed descriptions of all geometry optimized structures are in the Supporting Information.

The overall gas phase room temperature decomposition of **1** proceeding through sequential eliminations of DME, fluoroisobutylene, and the hexafluoro-*tert*-butanol to initiation of aggregation of the oxide matrix could be highly exergonic with $\Delta G = -54.2$ kcal mol^{-1} ($\Delta H = -28.9$ kcal mol^{-1}) with respect to the ground state **1**. The kinetic barrier for dissociation of the DME in **1** ($\Delta G = +22.8$ kcal mol^{-1}, $\Delta H = +33.8$ kcal mol^{-1}) is

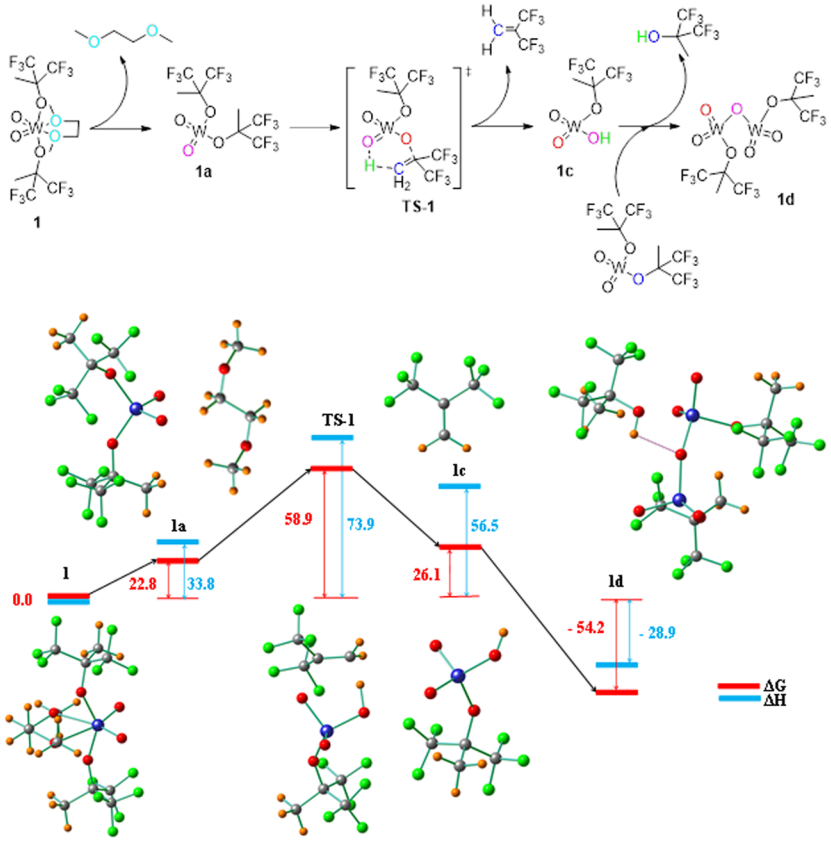

Figure 5. Energy profile (ΔG and ΔH, in kcal mol^{-1}) for possible mechanistic steps for loss of DME, hexafluoroisobutylene, and hexafluoro-*tert*-butanol from **1**.

DOI: 10.1021/acs.inorgchem.5b01124
Inorg. Chem. 2015, 54, 7536−7547

of a reasonable magnitude for a reaction occurring under the film deposition conditions. The coordinatively unsaturated four coordinate **1a** proceeds to a cyclic transition state (**TS-1**) involving intramolecular proton abstraction by a terminal oxo group ($\Delta G^{\ddagger}$ = 58.9 kcal mol^{-1} and $\Delta H^{\ddagger}$ = 73.9 kcal mol^{-1}). Intermediate **1c** is generated via release of hexafluoroisobutylene from **TS-1**. The terminal hydroxide group in **1b** promotes efficient dimerization through **1c** that undergoes a subsequent step to release a hexafluoro-*tert*-butanol.

The related mono-oxo complex **4** can undergo decomposition to **1a** through a pathway involving intramolecular abstraction of a methyl proton by the oxygen atom of an adjacent fluoroalkoxide to generate **TS-4** with calculated energies of $\Delta G^{\ddagger}$ = 28.3 kcal mol^{-1} and $\Delta H^{\ddagger}$ = 27.8 kcal mol^{-1}.

Compared with activation of **1a** to **TS-1** (Figure 5), the initial activation of **4** to **TS-4** (Scheme 4) is lower in energy

Scheme 4. Possible Mechanistic Steps for Formation of 1a from 4

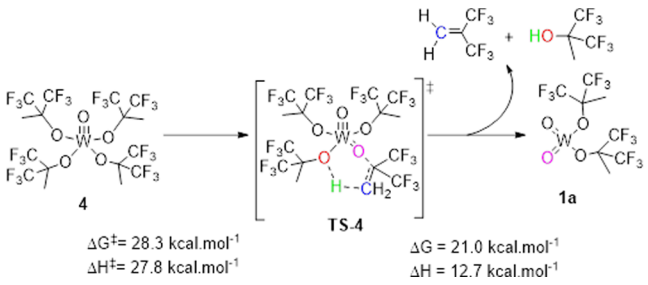

($\Delta\Delta G^{\ddagger}$ = −7.8 kcal mol^{-1} and $\Delta\Delta H^{\ddagger}$ = −12.3 kcal mol^{-1}). Conversion of **4** to film could thus proceed via **1a**. If **1a** is indeed a common intermediate in depositions of WO_x from **1** and **4**, then the two precursors should show similar behavior during film growth.

WO_x Material Properties. WO_x materials were grown using **1** as a single-source precursor in diglyme or DME, with additional experiments involving water as a coreactant when using diglyme. In all cases, N_2 was used as the carrier gas. Although F is present in the precursor, no fluorine was detected in the WO_x samples by XPS either before or after sputtering.

As a base study, material was deposited with **1** under single-source conditions in diglyme in the temperature range 150 to 550 °C. The films were then characterized to determine the elemental composition (XPS), thickness and thus growth rate (SEM), growth habits (SEM, AFM), phase constitution (XRD) as well as the electrical conductivity (4 point probe), work function (UPS), and optical transmittance. The most striking result from the characterization studies is a change in growth habit as temperature is increased. Materials deposited in the temperature range 150 to 300 °C show continuous growth of amorphous film, which then transitions to highly textured crystalline nanorod morphology in the temperature range 350 to 550 °C. Similar studies were performed using a different solvent (DME) or adding H_2O as a coreactant, and the same change in growth mode was observed. Additionally, the solvent influences the nanorod growth process, while supplying water dramatically affects the growth rate in the low temperature range and modifies the nanorod electrical properties. The detailed results of changing the growth temperature and solvent and adding H_2O as coreactant on the growth process and material properties are presented next.

The elemental composition as a function of growth temperature for each solvent/H_2O condition is shown in Figure 6a, while Figure 6b tracks the O:W atomic ratio. When

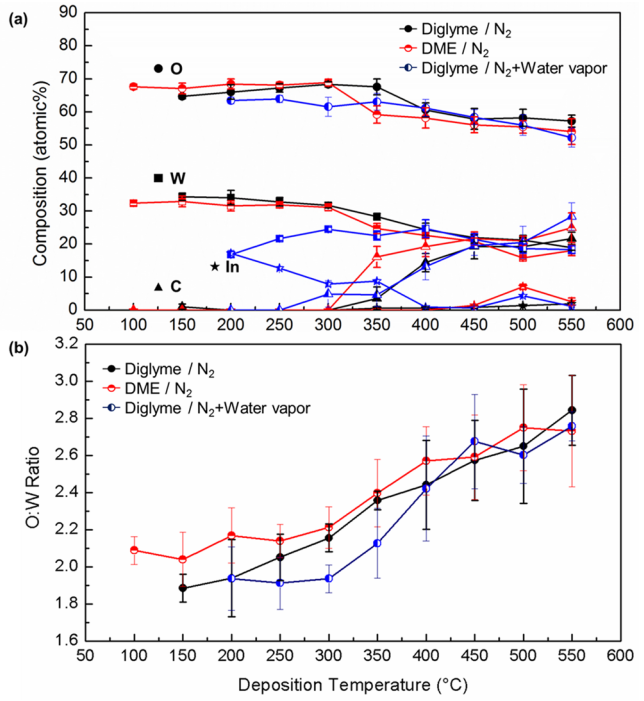

Figure 6. (a) Elemental composition (XPS) versus deposition temperature, and (b) oxygen to tungsten atom ratio of materials grown from **1** at different temperatures using either diglyme or DME solvent and N_2 or N_2 and water vapor. Note that a small amount of Sn (<3 atom %) was detected in samples in which In was detected.

using **1** under single-source conditions in either solvent, Figure 6a shows films deposited between 150 and 300 °C are essentially C-free and the O:W atomic ratio gradually increases (e.g., O:W for **1** in diglyme increases from 1.89 to 2.16), consistent with more oxygen-rich WO_x. With the addition of H_2O in this lower temperature range the W content gradually increases as deposition temperature increases, while the O content is relatively constant. In the high-temperature nanorod growth regime (350 to 550 °C), composition differences between choices of solvent and added H_2O become small. The most notable change is increasing C level with increasing temperature, particularly during use of DME. The carbon concentration increases from 4 atom % C for samples grown at 350 °C to as high as 22 atom % at 550 °C. C exists as an impurity, and its presence at high temperature (350−550 °C) is consistent with decomposition of the precursor and/or solvent to generate carbon containing fragments. Furthermore, at high temperatures, a nanorod growth morphology develops that provides a significantly higher surface area for adsorption of both atmospheric and reaction produced C species, inflating its content in the material. To better understand whether the C resides on the surface or in the bulk nanorod, the 350 °C sample was Ar-ion sputtered for 10 min and then the surface concentration was measured using XPS. The carbon level decreased from 27 to 4 atom %, consistent with carbon primarily located on the surface.

Low In levels are present (1−2 atom %) in material deposited at high temperatures (≥350 °C), which is consistent

DOI: 10.1021/acs.inorgchem.5b01124
Inorg. Chem. 2015, 54, 7536−7547

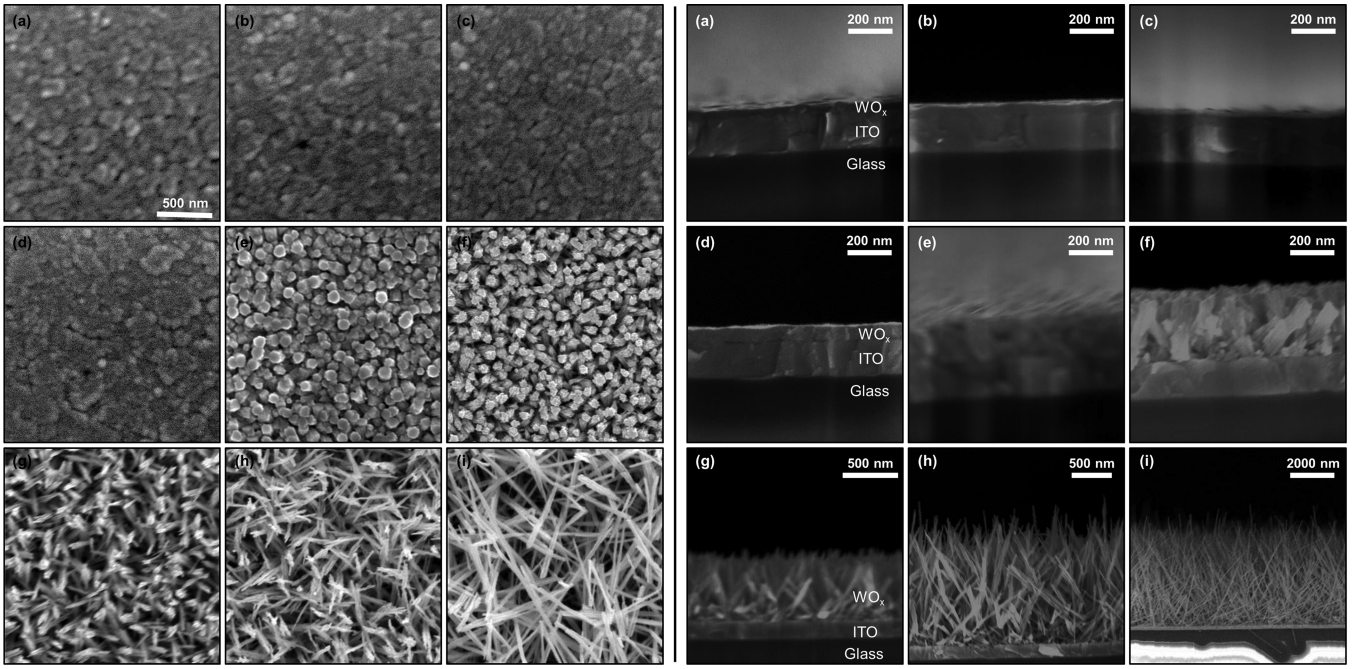

Figure 7. Plan-view (left) and cross-sectional (right) SEM images of materials grown from **1** at (a) 150, (b) 200, (c) 250, (d) 300, (e) 350, (f) 400, (g) 450, (h) 500, and (i) 550 °C with diglyme in N_2 atmosphere. Note that the plan-view images are at the same magnification and the cross-sectional images are of varying magnification as indicated.

with exposure of the underlying ITO substrate upon change in the material morphology (see Figure 7). The oxygen to tungsten ratio (O:W ratio) shown in Figure 6b increases from 1.9 to 2.8 as the deposition temperature increases from 150 to 550 °C. These results are consistent with those of previously investigated tungsten(VI) mono-oxo alkoxide precursors, **3** and **4**, under similar growth conditions,[43] providing further evidence for a common intermediate in deposition from the mono- and dioxo precursors.

There is little difference in the tungsten oxide grown from single-source conditions using DME and diglyme solutions of **1**. However, materials grown in the presence of coreactant H_2O at low temperatures (200−350 °C) show significant In and Sn levels, varying from 17 to 8 atom % and 3 to 1 atom %, respectively, which yield values of the In:Sn atomic ratio close to the 9:1 ratio in the initial ITO layer. This may indicate that the deposit is thinner than the escape depth of the observed photoelectrons and/or there is incomplete substrate coverage, as seen in SEM images (Figure S27 in the Supporting Information). At higher temperatures (400−550 °C) the film compositions are similar for all experimental conditions.

Surface morphologies and cross-sectional images of materials grown from diglyme solutions of **1** under single-source conditions at different temperatures are compared in Figure 7. The SEM images exhibit two distinct morphologies: WO_x thin films at low temperatures (150−300 °C) and nanorods at high temperatures (350−550 °C). The oxide films grown at low temperatures show similar compositions and the SEM images in Figure 7 reveal film thickness increasing with temperature. In contrast the XPS data of nanorods show enhanced C incorporation and reduced O. Furthermore, the SEM images in Figure 7 show significant increase in the rod length but reduction in the diameter (e.g., the nanorods grown at 400 °C have 40−100 nm diameter and are 337 ± 10 nm in length, whereas at 550 °C the diameter and length are 20−50 nm and 4.8 ± 0.3 μm, respectively). It is also noted that the nanorods exhibit similar preferred growth in the [010] direction. These structures were also observed for material grown from **3** and **4** at the same deposition temperatures.[43] The WO_x materials grown from DME solutions of **1** experience nearly identical morphological trends (Figure S26 in the Supporting Information), however, the nanorod dimensions were affected by solvent selection. The nanorods grown from DME solutions have smaller diameters and are shorter in length than the materials grown from diglyme. Comparing the nanorod dimensions cited previously for use of diglyme solutions, those grown with DME at 400 °C have dimensions of 30−80 nm diameter and 242 ± 11 nm length, and those deposited at 550 °C are 20−50 nm and 3.9 ± 0.3 μm in diameter and length, respectively (Table S8 in the Supporting Information).

In contrast, WO_x films grown in the presence of coreactants have different features at low deposition temperatures (Figure S27 in the Supporting Information). The SEM micrographs show that films grown at 200 and 250 °C have thickness less than 20 nm, increasing only slightly to 31 nm at 300 °C. Films grown at 300 °C are also rougher than those grown at lower temperature. It is noted that incomplete substrate coverage was detected between the short and thin nanorods at 350 °C. These features are consistent with the In and Sn observed via XPS at these growth temperatures. Nanorods grown with H_2O added at high temperatures (450−550 °C), however, have similar nanorod number density, diameter, and length as those under single-source conditions.

The film and nanorod growth rates were estimated from the film thickness or nanorod mean length, respectively, as determined by the cross-sectional imaging, divided by the total deposition time. The film and nanorod growth rate dependence on reciprocal deposition temperature are shown in the Arrhenius plots in Figures 8a and 8b, respectively. For films

DOI: 10.1021/acs.inorgchem.5b01124
Inorg. Chem. 2015, 54, 7536−7547

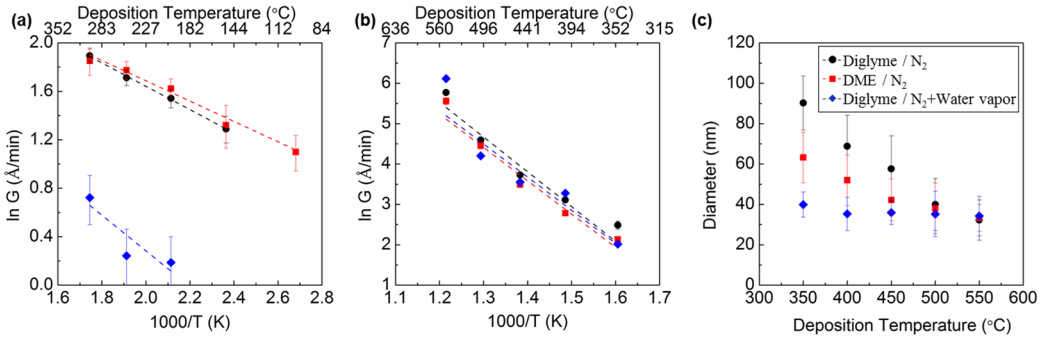

Figure 8. Variation of deposition rate from **1** and nanorod diameter as a function of temperature: (a) film growth rate vs inverse deposition temperature in low temperature regime; (b) nanorod tip growth rate vs inverse deposition temperature in high temperature regime; and (c) nanorod diameter vs growth temperature in high temperature regime.

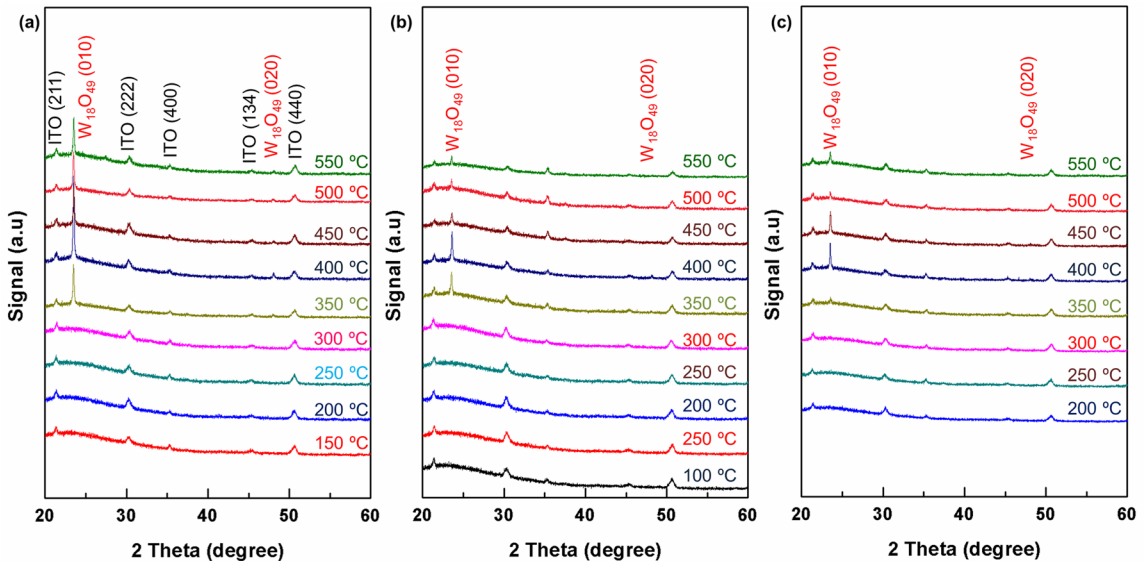

Figure 9. XRD spectra for WO_x materials grown from **1** with (a) diglyme/N_2, (b) DME/N_2, and (c) diglyme/N_2 and water vapor.

grown under single-source conditions at low deposition temperatures (150−300 °C), the growth rates and the apparent activation energy are almost identical with estimated activation energy of 0.08 ± 0.01 eV [1.9 ± 0.2 kcal mol^{-1}] and 0.07 ± 0.01 eV [1.7 ± 0.2 kcal mol^{-1}] for diglyme and DME solutions, respectively. These very low activation energies suggest that growths are mass transfer limited as kinetic limitations often produce values ranging from 0.5 to 1 eV [11.5 to 23.1 kcal mol^{-1}].[54] Interestingly, these values are much lower than values for thin film growth from **3** and **4** at similar temperatures: 0.22 ± 0.02 eV [5.1 ± 0.5 kcal mol^{-1}] and 0.34 ± 0.02 eV [7.8 ± 0.5 kcal mol^{-1}], respectively. It was asserted that the growth rate of **3**, which was experimentally determined to be proportional to the square root of the carrier gas flow rate, was also mass transfer limited. However, a change in activation energy between the film and the nanorod growth regime was not observed with those previous precursors.[43] A key observation is that when water vapor was introduced, film growth rates were much slower. For example, the growth rate of the film grown at 200 °C in the presence of water was 1.2 ± 0.3 Å/min compared to 4.7 ± 0.4 Å/min under single-source conditions (Table S8 in the Supporting Information). These observations are consistent with reports that the rate for TiO_2 film growth via CVD decreases as water vapor pressure increases because of competition between precursor and coreactant for reaction sites.[55]

The Arrhenius plots for nanorods grown at high temperatures (350−550 °C) yield similar activation energies of 0.70 ± 0.01, 0.74 ± 0.01, and 0.79 ± 0.01 eV [16.2 ± 0.2, 17.1 ± 0.2, and 18.3 ± 0.1 kcal mol^{-1}], for each growth condition of diglyme (single-source), DME (single-source), and diglyme (H_2O coreactant), respectively. The growth of nanorods at 450−550 °C from the previous precursors **3** and **4** under the same growth conditions shows higher apparent activation energies of 1.13 ± 0.02 and 0.86 ± 0.01 eV [26.1 ± 0.5 and 19.8 ± 0.2 kcal mol^{-1}], respectively. These high activation energies and uniform rod diameter suggest that the rate determining growth step may be surface reaction on the nanorod tips and possible reaction and diffusion along the side wall. The computational data (Figure 5 and Scheme 4) are consistent with rapid decomposition of **4** to **1a**. Because a common intermediate (**1a**) is involved and it is formed before the rate-determining step for film growth, the differences between the structures of mono-oxo complex **4** and its tungsten(VI) dioxo derivative **1** are not significant in the kinetics of WO_x growth.

In the nanorod growth regime at higher temperatures (350 to 550 °C) for growth from **1**, the diameter of each rod was uniform and constant at a given growth temperature. With

DOI: 10.1021/acs.inorgchem.5b01124
Inorg. Chem. 2015, 54, 7536−7547

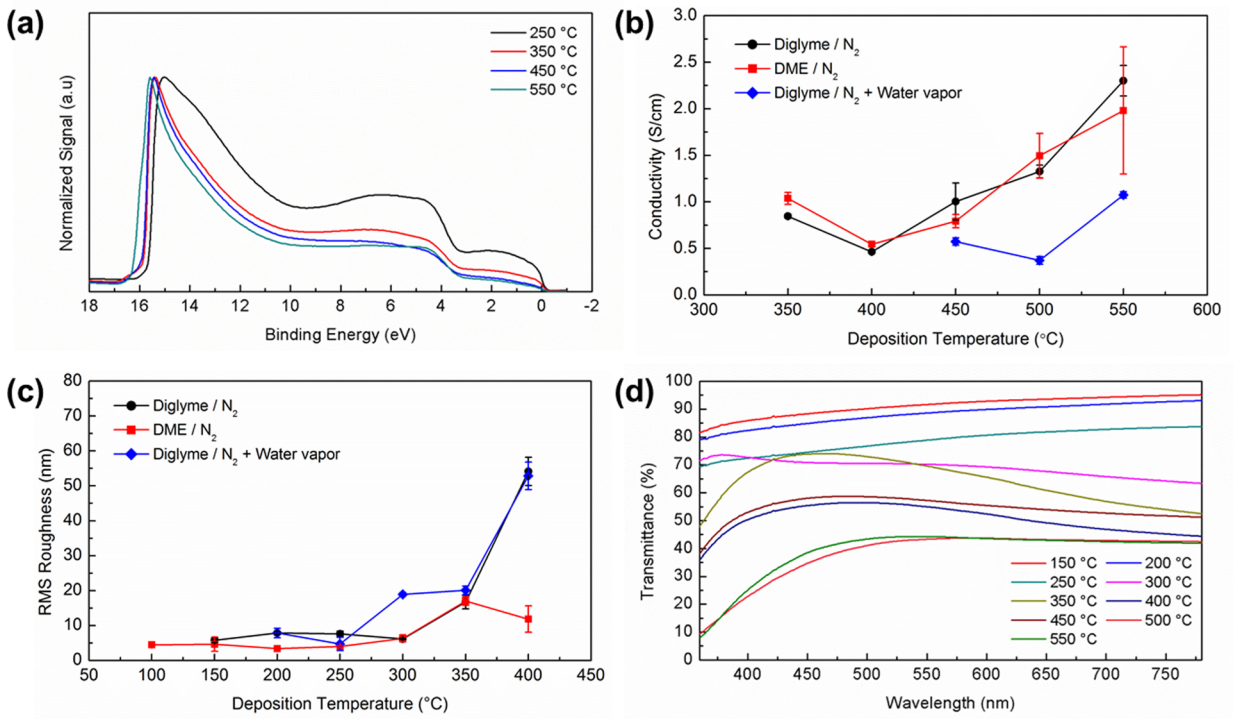

Figure 10. (a) UPS spectra, (b) electrical conductivities, (c) RMS surface roughness, and (d) visible light transmittance of tungsten oxides grown from **1** in various conditions.

increasing growth temperature the nanorod diameter decreases (Figure 8c) and the nanorod length increases (Figures 7 and 8b) for the same growth time and reactant feed rate. The choice of solvent and addition of H_2O have minimal impact on the length of the nanorod (Figure 8b), however, the diameter of the nanorod depends on the solvent and presence of coreactant H_2O (Figure 8c). The data show that the diameter decreases with increasing temperature but the magnitude of the diameter and the change with increasing temperature depend on the solvent/coreactant. Use of diglyme/N_2 gives the largest diameter and temperature sensitivity (diameter decreases from 90 ± 13 to 32 ± 10 nm), followed by DME/N_2 (diameter decreases from 63 ± 13 to 33 ± 7 nm diameter), and then diglyme/N_2 + H_2O (diameter decreases from 40 ± 6 to 34 ± 10 nm diameter). It is noted that the diameter converges to the same value at 550 °C (Figure S28 in the Supporting Information), consistent with a common nucleation mechanism. There are previous studies of WO_x nanorod growth by different precursors and processes in approximately the same temperature range. It was reported that thick bundled $W_{18}O_{49}$ nanotubes grown at 530 °C by flame vapor deposition using a WO_x vapor source become thin nanowires at 700 °C,[56] and that WO_x grown from a $W(OPh)_6$ solution by AACVD transforms from granular at 350 °C to needle-like at 500 °C.[57] In contrast, the nanorods grown from diglyme solutions of **1** in the presence of water vapor minimally change in diameter.

The XRD patterns of WO_x films grown from **1** at low temperatures under all three conditions show only ITO reflections and a broad peak at low angles from the amorphous glass substrate (Figure 9), consistent with the growth of thin amorphous WO_x. With the onset of nanorod growth at higher deposition temperatures (≥350 °C), two distinct diffraction peaks emerge at 23.5 and 48.0° 2θ that are assigned to the monoclinic $W_{18}O_{49}$ (010) and (020) planes. This phase has been identified previously in films grown by different methods, including thermal evaporation of WO_3 powder and a solvothermal method using tungsten chloride and cyclohexanol as precursors.[30,58,59] The monoclinic $W_{18}O_{49}$ unit cell lattice parameters are a = 18.324, b = 3.784, and c = 14.035 Å and β = 115.2°.[60] The Bravais–Friedel–Donnay–Harker (BFDH) law states that the crystalline growth direction with the shortest d-spacing, in this case the [010] direction, has the fastest growth rate.[61,62] In addition, {010} planes have oxygen vacancies that can serve as chemisorption sites for precursor species and therefore encourage growth.[63]

To use tungsten oxide thin films and nanorods as buffer layers or gas sensors, their work function, electrical conductivity, surface roughness, and visible light transmittance are critical properties. Figure 10a shows Fermi-level aligned UPS spectra of WO_x grown from single-source diglyme solutions of **1** at 250, 350, 450, and 550 °C, with estimated work function values of 5.6, 5.4, 5.3, and 4.9 eV, respectively. These values are greater than the measured work function of the underlying ITO substrate (4.2–4.3 eV) but lower than reported work functions for WO_3 (6.2–6.7 eV).[3,8] This is likely due to defect energy states above the valence band related to oxygen deficiency. The most intense peak around 15.5 eV arises from secondary electrons escaping from the surface. The second most intense peak around 4.5 eV comes from O 2p states in the oxide valence band. The smallest peak from 0 to 3 eV arises from oxygen vacancy defects in the oxide network due to electron occupation of the W 5d states.[64] The decreasing work function with increasing deposition temperature may result from C incorporation.

A comparison of electrical conductivity between materials obtained under the three different growth conditions is provided in Figure 10b. Electrical conductivities of materials on plain glass were calculated from the sheet resistance, as

DOI: 10.1021/acs.inorgchem.5b01124
Inorg. Chem. 2015, 54, 7536–7547

measured by 4 point probe, and material thickness determined from cross-sectional SEM imaging. Tungsten oxide films grown at low temperatures were highly resistive, exceeding the equipment measurement range (>100 kΩ/square). The tungsten oxide nanorods grown without water vapor have electrical conductivities varying from 0.5 to 2.3 S/cm that increase with deposition temperature regardless of solvent. In comparison, the electrical conductivity of $W_{18}O_{49}$ has been reported to be 2.58 S/cm for nanowires and 4 S/cm for bulk materials.[65,66] Tungsten oxide nanorods grown with water vapor show relatively low electrical conductivities in the range of 0.4−1.1 S/cm. The oxygen vacancies of WO_x contribute to its semiconductivity, and some dissociation of H_2O on defect sites of tungsten oxide may reduce the oxygen vacancy concentration of the material grown with water vapor.[67,68]

The surface roughness values of grown materials were measured by AFM (Figure 10c). The tungsten oxide films grown from 100 to 300 °C under various conditions have roughness values ranging from 3.4 ± 0.2 to 7.9 ± 1.3 nm, which are approximately that of the ITO substrate (3.8 ± 0.1 nm). However, as the morphology transitions to vertical nanorods, the surface roughness as measured by AFM increases to 54.1 ± 4.0 nm at 400 °C (SEM images in Figure 7f).

The transmittances of materials were measured by UV−vis spectroscopy. The visible light transparencies of tungsten oxide grown on bare glass from **1** distilled in diglyme under N_2 are shown in Figure 10d. The mean transmittance decreases from 91.1 to 39.1% as the deposition temperature increases from 150 to 550 °C. This corresponds to the increasing material thickness as well as coloration induced by the $W_{18}O_{49}$ structure.[12,69] The nanorod material, compared to films grown at high temperatures (350−450 °C), shows higher transmittance values at wavelengths around 470−490 nm, which corresponds to blue light. $W_{18}O_{49}$ nanorods can experience a strong quantum confinement effect and contain oxygen defects, which can prevent blue light absorption.[12,69] However, when the thicknesses of the tungsten oxide materials are normalized to 10 nm (the industry stipulated maximum thickness), the overall visible light transmittances (Figure S29 in the Supporting Information) are higher than 98% for all conditions.

CONCLUSIONS

The dioxo fluoroalkoxide tungsten(VI) complexes $WO_2(OR)_2(DME)$ [**1**; R = $C(CF_3)_2CH_3$; **2**, $C(CF_3)_3$] have been synthesized as precursors for AACVD of WO_x and characterized by NMR, X-ray crystallography, and mass spectrometry. TGA and variable temperature NMR data confirm that the complexes are temperature and solvent sensitive. DFT calculations are consistent with gas phase decomposition of **1** and **4** occurring through a common intermediate (**1a**). Materials grown from both precursors were similar, which suggests that the differences in the molecular structure for **1** and **4** are not significant to the overall materials' growth characteristics during CVD with these precursors. Complex **1** was shown to be a viable single-source precursor for growth of uniform and robust thin films of substoichiometric amorphous WO_x on ITO covered glass and borosilicate glass substrates heated between 100 and 300 °C. Above 300 °C, crystalline monoclinic $W_{18}O_{49}$ nanorods were obtained. The as-grown WO_x film work function and conductivity were shown to vary from 4.9 to 5.6 eV and 0.4 to 2.3 S/cm with deposition temperature, respectively. A normalized optical transmittance over 98% could be realized for all growth conditions. The observed properties indicate that the WO_x thin films grown by AACVD of **1** are suitable for charge-injection purposes.

ASSOCIATED CONTENT

Supporting Information

Experimental details for thermolysis of **1** and **2**, NMR spectra for **1** and **2** and their thermolysis products, MS data for **1** and **2** and their thermolysis products, crystal data and structure refinement for **1** and **2**, atomic coordinates and equivalent isotropic displacement parameters for **1** and **2**, bond lengths and angles for **1** and **2**, detailed procedure for DFT calculations, optimized geometries and Cartesian coordinates for species calculated to be on the pathway toward decomposition of **1** and **4**, schematic of AACVD system, SEM images of materials grown from DME solution of **1** in N_2 and diglyme solution of **1** in N_2 containing water vapor, dimensions of nanorods, and transmittance of 10 nm WO_x grown from diglyme solution of **1** in N_2. The Supporting Information is available free of charge on the ACS Publications website at DOI: 10.1021/acs.inorgchem.5b01124.

AUTHOR INFORMATION

Corresponding Author

*E-mail: lmwhite@chem.ufl.edu.

Author Contributions

R.O.B. and H.K. contributed equally to the writing of this manuscript.

Notes

The authors declare no competing financial interest.

ACKNOWLEDGMENTS

The authors would like thank the National Science Foundation for support under the GOALI Grant CHE-1213965. K.A.A. wishes to acknowledge the National Science Foundation and the University of Florida for funding of the purchase of the X-ray equipment.

REFERENCES

(1) Wang, L.; Xu, W.; Luo, Y.; Yuan, J.; Ding, Y. *Displays* **2011**, *32*, 45.
(2) Dinh, N. N.; Chung, D. N.; Thao, T. T.; Thuy, T. T. C.; Chi, L. H.; Truong, V.-V. *Mater. Sci. Appl.* **2013**, *4*, 275.
(3) Meyer, J.; Hamwi, S.; Kroger, M.; Kowalsky, W.; Riedl, T.; Kahn, A. *Adv. Mater.* **2012**, *24*, 5408.
(4) Zhong, J. Q.; Mao, H. Y.; Wang, R.; Lin, J. D.; Zhao, Y. B.; Zhang, J. L.; Ma, D. G.; Chen, W. *Org. Electron.* **2012**, *13*, 2793.
(5) Deb, S. K. *Sol. Energy Mater. Sol. Cells* **2008**, *92*, 245.
(6) Vasilopoulou, M.; Palilis, L. C.; Georgiadou, D. G.; Argitis, P.; Kennou, S.; Kostis, I.; Papadimitropoulos, G.; Stathopoulos, N. A.; Iliadis, A. A.; Konofaos, N.; Davazoglou, D.; Sygellou, L. *Thin Solid Films* **2011**, *519*, 5748.
(7) Vasilopoulou, M.; Papadimitropoulos, G.; Palilis, L. C.; Georgiadou, D. G.; Argitis, P.; Kennou, S.; Kostis, I.; Vourdas, N.; Stathopoulos, N. A.; Davazoglou, D. *Org. Electron.* **2012**, *13*, 796.
(8) Meyer, J.; Winkler, T.; Hamwi, S.; Schmale, S.; Johannes, H.-H.; Weimann, T.; Hinze, P.; Kowalsky, W.; Riedl, T. *Adv. Mater.* **2008**, *20*, 3839.
(9) Acharya, R.; Cao, X. A. *Appl. Phys. Lett.* **2012**, *101*, 053306/1.
(10) Li, J.; Yahiro, M.; Ishida, K.; Yamada, H.; Matsushige, K. *Synth. Met.* **2005**, *151*, 141.
(11) Vasilopoulou, M.; Palilis, L. C.; Georgiadou, D. G.; Douvas, A. M.; Argitis, P.; Kennou, S.; Sygellou, L.; Papadimitropoulos, G.; Kostis,

DOI: 10.1021/acs.inorgchem.5b01124
Inorg. Chem. 2015, 54, 7536−7547

I.; Stathopoulos, N. A.; Davazoglou, D. *Adv. Funct. Mater.* **2011**, *21*, 1489.
(12) Xi, G.; Ouyang, S.; Li, P.; Ye, J.; Ma, Q.; Su, N.; Bai, H.; Wang, C. *Angew. Chem., Int. Ed.* **2012**, *51*, 2395.
(13) Migas, D. B.; Shaposhnikov, V. L.; Borisenko, V. E. *J. Appl. Phys.* **2010**, *108*, 093714.
(14) Migas, D. B.; Shaposhnikov, V. L.; Rodin, V. N.; Borisenko, V. E. *J. Appl. Phys.* **2010**, *108*, 093713.
(15) Kim, J. H.; Lee, Y. J.; Jang, Y. S.; Jang, J. N.; Kim, D. H.; Song, B. C.; Lee, D. H.; Kwon, S. N.; Hong, M. *Org. Electron.* **2011**, *12*, 285.
(16) Rout, C. S.; Hegde, M.; Rao, C. *Sens. Actuators, B* **2008**, *128*, 488.
(17) Wang, C.; Yin, L.; Zhang, L.; Xiang, D.; Gao, R. *Sensors* **2010**, *10*, 2088.
(18) Hong, K. Q.; Xie, M. H.; Hu, R.; Wu, H. S. *Nanotechnology* **2008**, *19*, 085604.
(19) Qian, J.; Peng, Z.; Wu, D.; Fu, X. *Key Eng. Mater.* **2014**, *602*−*603*, 51.
(20) Hou, X.; Choy, K. L. *Chem. Vap. Deposition* **2006**, *12*, 583.
(21) Marchand, P.; Hassan, I. A.; Parkin, I. P.; Carmalt, C. J. *Dalton Trans.* **2013**, *42*, 9406.
(22) Vallejos, S.; Umek, P.; Blackman, C. *J. Nanosci. Nanotechnol.* **2011**, *11*, 8214.
(23) Riaz, U. *Thin Solid Films* **1993**, *235*, 15.
(24) Piccirillo, C.; Binions, R.; Parkin, I. P. *Thin Solid Films* **2008**, *516*, 1992.
(25) Basato, M.; Brescacin, E.; Tondello, E. *Chem. Vap. Deposition* **2001**, *7*, 219.
(26) Cross, W. B.; Parkin, I. P.; O'Neill, S. A.; Williams, P. A.; Mahon, M. F.; Molloy, K. C. *Chem. Mater.* **2003**, *15*, 2786.
(27) Cross, W. B.; Parkin, I. P.; White, A. J. P.; Williams, D. J. *Dalton Trans.* **2005**, 1287.
(28) Baxter, D. A.; Chisolm, M. H.; Doherty, S.; Gruhn, N. E. *Chem. Commun.* **1996**, 1129.
(29) Molloy, K. C.; Williams, P. A. *Appl. Organomet. Chem.* **2008**, *22*, 676.
(30) Bonsu, R. O.; Kim, H.; O'Donohue, C.; Korotkov, R. Y.; McClain, K. R.; Abboud, K. A.; Ellsworth, A. A.; Walker, A. V.; Anderson, T. J.; McElwee-White, L. *Dalton Trans.* **2014**, *43*, 9226.
(31) Molloy, K. C.; Williams, P. A. *Appl. Organomet. Chem.* **2008**, *22*, 560.
(32) Won, Y. S.; Kim, Y. S.; Anderson, T. J.; McElwee-White, L. *Chem. Mater.* **2008**, *20*, 7246.
(33) Won, Y.; Kim, Y.; Anderson, T.; Reitfort, L.; Ghiviriga, I.; McElwee-White, L. *J. Am. Chem. Soc.* **2006**, *128*, 13781.
(34) Terry, K. W.; Tilley, T. D. *Chem. Mater.* **1991**, *3*, 1001.
(35) Terry, K. W.; Ganzel, P. K.; Tilley, T. D. *Chem. Mater.* **1992**, *4*, 1290.
(36) Buono-Core, G. E.; Klahn, A. H.; Castillo, C.; Bustamante, M. J.; Munoz, E.; Cabello, G.; Chornik, B. *Polyhedron* **2011**, *30*, 201.
(37) Buono-Core, G. E.; Klahn, A. H.; Cabello, G.; Munoz, E.; Bustamante, M. J.; Castillo, C.; Chornik, B. *Polyhedron* **2012**, *41*, 134.
(38) Pedersen, F. S.; Schrock, R. R. *J. Am. Chem. Soc.* **1982**, *104*, 7483.
(39) Dreisch, K.; Andersson, C.; Staalhandske, C. *Polyhedron* **1991**, *10*, 2417.
(40) Samuels, J. A.; Folting, K.; Huffman, J. C.; Caulton, K. G. *Chem. Mater.* **1995**, *7*, 929.
(41) *SHELXTL2013*; Bruker-AXS: Madison, WI, 2013.
(42) *SHELXTL6*; Bruker-AXS: Madison, WI, 2008.
(43) Kim, H.; Bonsu, R. O.; O'Donohue, C.; Korotkov, R. Y.; McElwee-White, L.; Anderson, T. J. *ACS Appl. Mater. Interfaces* **2015**, *7*, 2660.
(44) Interrante, L. V.; Han, B.; Hudson, J. B.; Whitmarsh, C. *Appl. Surf. Sci.* **1990**, *46*, 5.
(45) Jones, A. C.; Aspinall, H. C.; Chalker, P. R. *Surf. Coat. Technol.* **2007**, *201*, 9046.
(46) Doppelt, P. *Coord. Chem. Rev.* **1998**, *178*−*180*, 1785.
(47) Devi, A. *Coord. Chem. Rev.* **2013**, *257*, 3332.
(48) McElwee-White, L. *Dalton Trans.* **2006**, 5327.
(49) Miinea, A. L.; Suh, S.; Hoffman, M. D. *Inorg. Chem.* **1999**, *38*, 4447.
(50) Samuels, J. A.; Lobkovsky, E. B.; Streib, W. E.; Folting, K.; Huffman, J. C.; Zwanziger, J. W.; Caulton, K. G. *J. Am. Chem. Soc.* **1993**, *115*, 5093.
(51) Buchanan, W. D.; Guino-O, M. A.; Ruhlandt-Senge, K. *Inorg. Chem.* **2010**, *49*, 7144.
(52) Jarupatrakorn, J.; Coles, M. P.; Tilley, T. D. *Chem. Mater.* **2005**, *17*, 1818.
(53) Brower, D. C.; Templeton, J. L.; Mingos, D. M. P. *J. Am. Chem. Soc.* **1987**, *109*, 5203.
(54) Raaijmakers, I. J.; Yang, J. *Appl. Surf. Sci.* **1993**, *73*, 31.
(55) Wang, W. B.; Yanguas-Gil, A.; Yang, Y.; Kim, D.-Y.; Girolami, G. S.; Abelson, J. R. *J. Vac. Sci. Technol., A* **2014**, *32*, 061502.
(56) Rao, P. M.; Cho, I. S.; Zheng, X. *Proc. Combust. Inst.* **2013**, *34*, 2187.
(57) Stoycheva, T.; Vallejos, S.; Blackman, C.; Moniz, S. J. A.; Calderer, J.; Correig, X. *Sens. Actuators, B* **2012**, *161*, 406.
(58) Sun, S.; Zhao, Y.; Xia, Y.; Zou, Z.; Min, G.; Zhu, Y. *Nanotechnology* **2008**, *19*, 305709.
(59) Huang, K.; Pan, Q. T.; Yang, F.; Ni, S. B.; He, D. Y. *Appl. Surf. Sci.* **2007**, *253*, 8923.
(60) Booth, J.; Ekstroem, T.; Iguchi, E.; Tilley, R. J. D. *J. Solid State Chem.* **1982**, *41*, 293.
(61) Frey, G. L.; Rothschild, A.; Sloan, J.; Rosentsveig, R.; Popovitz-Biro, R.; Tenne, R. *J. Solid State Chem.* **2001**, *162*, 300.
(62) Donnay, J. D. H.; Harker, D. *Am. Mineral.* **1937**, *22*, 446.
(63) Smith, A. M.; Kast, M. G.; Nail, B. A.; Aloni, S.; Boettcher, S. *J. Mater. Chem. A* **2014**, *2*, 6121.
(64) Greiner, M. T.; Helander, M. G.; Tang, W.-M.; Wang, Z.-B.; Qiu, J.; Lu, Z.-H. *Nat. Mater.* **2012**, *11*, 76.
(65) Salje, E.; Güttler, B. *Philos. Mag. B* **1984**, *50*, 607.
(66) Shi, S.; Xue, X.; Feng, P.; Liu, Y.; Zhao, H.; Wang, T. *J. Cryst. Growth* **2008**, *310*, 462.
(67) Gillet, M.; Lemire, C.; Gillet, E.; Aguir, K. *Surf. Sci.* **2003**, *532*−*535*, 519.
(68) Akbulut, M.; Sack, N. J.; Madey, T. E. *Surf. Sci.* **1996**, *351*, 209.
(69) Chen, Z.; Wang, Q.; Wang, H.; Zhang, L.; Song, G.; Song, L.; Hu, J.; Wang, H.; Liu, J.; Zhu, M.; Zhao, D. *Adv. Mater.* **2013**, *25*, 2095.

DOI: 10.1021/acs.inorgchem.5b01124
Inorg. Chem. 2015, 54, 7536−7547